Insight into the eigenmodes of plasmonic nanoclusters based on the Green's tensor method

Shourya Dutta-Gupta and Olivier J. F. Martin*

Nanophotonics and Metrology Laboratory (NAM), Swiss Federal Institute of Technology Lausanne (EPFL),
Lausanne CH-1015, Switzerland
*Corresponding author: olivier.martin@epfl.ch

Assemblies of plasmonic nanoparticles possess exotic properties that are used in numerous applications. Their efficiency for specific applications strongly depends on the modes supported by the structure. In this paper, we extend the Green's tensor formalism to compute the eigenmodes of an assembly of plasmonic nanoparticles. Using the developed technique, we investigate the specific cases of a nanoparticle monomer, dimer, and trimer. The influence of various geometrical parameters and of symmetry breaking on the eigenmodes of the assemblies is studied in detail, as well as the illumination conditions required to excite specific eigenmodes.   © 2015 Optical Society of America

OCIS codes: (250.5403) Plasmonics; (310.6628) Subwavelength structures, nanostructures; (350.4238) Nanophotonics and photonic crystals.

1. INTRODUCTION

Metallic nanostructures supporting plasmon resonances have been used in various applications such as SERS [1–5], biosensing [6–9], plasmonic trapping [10–12], and fluorescence enhancement [13–18]. Optimization of a plasmonic structure for a particular application is made easier via the use of various computational tools. Most numerical techniques such as the FEM [19–21], the Green's tensor approach [22–24], discrete dipole approximation (DDA) [25,26], the boundary elements method (BEM) [27–30], and the surface integral equation (SIE) [31–33] compute the response of the structure due to an incident excitation.

In many situations, it is also beneficial or even necessary to determine the eigenmodes of the plasmonic system. Quite a few numerical techniques that compute the eigenmodes of a system are available [34–42]. For example, an electrostatic eigenmode solver based on the boundary integral equation was used to show that the near field of the plasmonic structures could be expressed as the linear superposition of the eigenmodes [42]. Knowledge of the modes and their relevance to the near field provided a simple method for the identification of hot spots necessary for plasmon enhanced spectroscopies. This approach can be extended a step further to control and localize hot spots in plasmonic aggregates through knowledge of the underlying plasmonic modal structure [43]. In contrast to techniques that compute the eigenmodes of a plasmonic structure by full numerical calculations, it is also possible to exploit symmetry properties by using group theory to study the interaction of an external electric field with the localized plasmon modes of the structure as shown by Zhang *et al.* [40]. With this approach, they showed that the selection rules for a vector field are different as compared to the selection rules for a scalar field. Knowledge of the eigenmodes of a plasmonic system can also be exploited

for increasing the accuracy and speed of a numerical technique [44]. However, it should be noted that the discretization of the structure necessary for computing the eigenmodes of the plasmonic structure using numerical techniques, even within the electrostatic limit, makes the solvers time consuming and memory intensive [41,42,45,46]. Furthermore, many of these techniques require initial guess values of the modes for accurate computation. On the other hand, for simple structures it is possible to exploit the symmetry of the structure to compute the modes using the dielectric constant as the eigenvalue of the system [40,47,48]. Even though eigenvalue analysis in the electrostatic approximation is easier and faster, the absence of retardation in the computation limits its applicability. In this paper, we extend the Green's tensor approach to compute the eigenmodes of a plasmonic structure composed of small nanoparticles. Our computation takes into account the retardation present between the nanoparticles. The developed technique is then used to analyze the eigenmodes of a nanoparticle monomer, dimer, and trimer.

The paper is organized as follows. In Section 2, we introduce the theoretical formalism used for computing the eigenmodes of a plasmonic system. In the next section, we study the eigenmodes of a single nanoparticle, a nanoparticle dimer, and a nanoparticle trimer. Finally, in Section 4, we present the main conclusions of the paper.

2. THEORETICAL FORMULATION

Consider a system of n nanoparticles placed in a background medium with dielectric constant ϵ_B. In systems where the particle size is significantly smaller than the wavelength of light, each nanoparticle can be represented by a single dipole with a finite polarizability [23]. In this paper, we assume that each nanoparticle is represented by a single dipole with an arbitrary orientation. The response of this generalized n

nanoparticle system can be calculated using the Green's tensor technique [22], where the field at each particle i is given by

$$\mathbf{E}_i = \mathbf{E}_i^0 + \sum_{j=1, j \neq i}^{n} \mathbf{G}_{ij} \cdot k_0^2 \Delta \epsilon_j V_j \mathbf{E}_j + \mathbf{M}_i \cdot \Delta \epsilon_i k_0^2 \mathbf{E}_i - \mathbf{L}_i \cdot \frac{\Delta \epsilon_i}{\epsilon_B} \mathbf{E}_i,$$
(1)

where $\mathbf{G}_{ij}$ is the background Green's tensor, k_0 is the vacuum wavenumber, $\Delta \epsilon_i (= \epsilon_i - \epsilon_B)$ is the dielectric constant contrast, $\mathbf{L}_i$ is the depolarization term, $\mathbf{M}_i$ is the self term, $\mathbf{E}_i^0$ is the incident field at dipole i, and V_i is the volume of the particle. In this equation the interaction between two interacting particles, i and j, is given by the tensor $\mathbf{G}_{ij}$, which depends on k_0. Since a single dipole is assigned to a single nanoparticle, the self-consistent fields computed using Eq. (1) also correspond to the dipole moments of the corresponding particles. This set of equations can be recast into the matrix form

$$(\mathbf{I} - \mathbf{S}) \cdot \mathbf{E} = \mathbf{E}^0,$$
(2)

where $\mathbf{I}$ is the identity matrix, $\mathbf{S}$ is the matrix that defines the system, and $\mathbf{E}^0$ and $\mathbf{E}$ are vectors corresponding to the incident fields and self-consistent electric fields at the dipoles, respectively.

The matrix $\mathbf{S}$ depends on the dielectric constant of the nanoparticle, and we use the Drude model given by

$$\epsilon = \epsilon_\infty - \frac{\omega_p^2}{\omega^2 + i \gamma \omega},$$
(3)

with $\epsilon_\infty = 9.5$, $\omega_p = 1.36 \cdot 10^{16}$ rad/s, and $\gamma = 1.05 \cdot 10^{14}$ rad/s [49]. These Drude parameters match well the experimentally measured dielectric function of gold in the 600–900 nm wavelength range. Additionally, more realistic models for the dielectric function that take into account the interband transitions in gold can also be used with this approach [50,51]. Note that the different terms of the matrix $\mathbf{S}$ also depend on the wavelength of light, because of the non-electrostatic nature of the current formalism. However, it must be pointed out that a direct relation exists between the dielectric function and the wavelength, and frequency, as given by the Drude model. For eigenmode computation of the system, we further enforce the condition that the incident field is zero. Therefore, Eq. (2) reduces to

$$(\mathbf{I} - \mathbf{S}) \cdot \mathbf{E} = \mathbf{0}.$$
(4)

The eigenmodes of this system can be determined by locating the parameters at which $\mathbf{E}$ is nonzero. Let $\xi(\lambda)$ be the eigenvalue of the matrix $\mathbf{S}$ at a given wavelength λ. It is evident that for $\xi(\lambda) = 1$, nonzero $\mathbf{E}$ is possible. The corresponding wavelengths are the eigenwavelengths of the system. In plasmonics, $\mathbf{S}$ is a complex matrix and the equation $\xi(\lambda) = 1$ is not satisfied for purely real λ. Therefore, in order to solve Eq. (4) a complex wavelength, $\lambda = \lambda_r + i \lambda_i$, must be assumed. The sign of the imaginary part of the eigenwavelengths is chosen to be positive for obtaining temporally decaying fields. Corresponding to this complex eigenwavelength, the complex eigenfrequency can be calculated using $\omega = 2\pi c / \lambda$, where c is the speed of light in vacuum. Such complex eigenwavelengths or eigenfrequencies are also found in other physical systems

such as damped harmonic oscillators [52] and RLC circuits [53]. The real and imaginary parts of the eigenwavelength of a mode correspond to the resonance position and half-width of the resonance, respectively [52]. The eigenvector of the matrix $\mathbf{S}$ at the eigenwavelength provides the electric field distribution for the given mode. Typical times required for computing the eigenmodes of the structures presented in this paper are in the range of 1 (for a nanoparticle monomer) to 10 min (for a nanoparticle trimer) when using a desktop computer with 4 GB memory.

3. RESULTS AND DISCUSSION

In this section, we first study the modes of a single nanoparticle as a function of the system parameters and show that the eigenmodes computed using the current formalism converge to the well-known quasi-static limit in plasmonics for small particles. Next, the modes of a symmetric nanoparticle dimer are computed, and its dependence on the system parameters investigated. Finally, we study the modes of a nanoparticle trimer, and the effects of symmetry breaking are illustrated via eigenmode analysis.

A. Single Nanoparticle

Consider a single gold nanoparticle embedded in a medium with $\epsilon_B = 6.145$. The refractive index of the background corresponds to the refractive index of TiO$_2$ [54]. For this system $\log_{10} |\xi - 1|$ as a function of λ_r and λ_i is shown in Fig. 1(a). It is clearly seen that $\xi = 1$ is satisfied for $\lambda = 662 + 14i$. Furthermore, at this wavelength the matrix $\mathbf{S}$ has an eigenvalue 1 with multiplicity 3; i.e., this eigenvalue is triply degenerate. Furthermore, the dipole moments corresponding to these triply degenerate eigenmodes are oriented along the x, y, and z directions. The degeneracy arises because all the axes are identical. Figures 1(b) and 1(c) show the variation of λ_r and λ_i as a function of particle size. As the particle size is increased from 4 to 30 nm, λ_r increases from 647 to 681 nm. Concurrently, the imaginary part of the eigenwavelength also shows a progressive increase as a function of the particle size. This increase in both the real and imaginary parts of the eigenwavelength as a function of size is due to the higher retardation effects for larger particles. Note that the retardation effects are taken into account by the presence of $k_0 R$ (R is the nanoparticle radius) terms present in the expressions for $\mathbf{G}_{ij}$ and $\mathbf{M}_i$. In this paper the wavelength is taken as the eigenvalue because of its widespread use in most plasmonic studies. However, calculations performed using frequency as the eigenvalue (shown in Appendix A) lead to exactly the same results. As mentioned previously, it is also possible to compute the dielectric constant corresponding to the eigenwavelength using the Drude model. This is useful since the dielectric constant is the preferred eigenvalue in most eigenmode analyses performed in the electrostatic limit [27,46,49]; hence, we plot the real (Re(ϵ)) and imaginary (Im(ϵ)) parts of the dielectric constant of gold at the eigenwavelengths [Figs. 1(d) and 1(e)]. Both Re(ϵ) and Im(ϵ) decrease upon increasing the size of the particle. Furthermore, ϵ approaches the well-known quasi-static limit $\epsilon = -2\epsilon_B$ in the case of 4 nm particles. Let us now consider the imaginary part of the dielectric constant at the eigenwavelength. Recall that the quasi-static limit arises when the denominator of the polarizability, which is proportional to $|(\epsilon - \epsilon_B)| / |(\epsilon + 2\epsilon_B)|$, is zero.
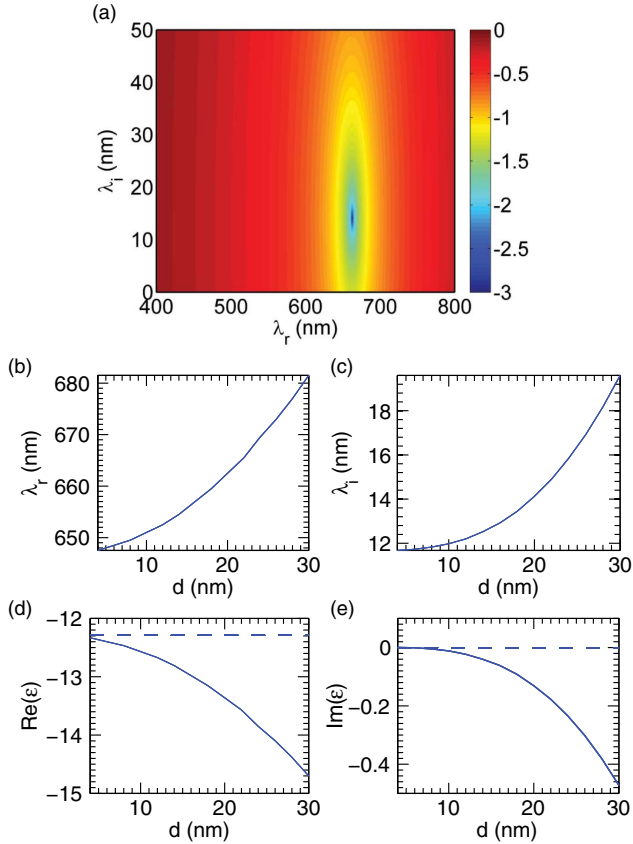
Fig. 1.   (a) $\log_{10}|\xi - 1|$ plotted as a function of the real and imaginary parts of wavelength, λ, for a 20 nm gold particle. (b) Real and (c) imaginary parts of the eigenwavelength for a single nanoparticle as a function of the particle size d. (d) Real and (e) imaginary parts of the dielectric constant of gold at the corresponding eigenwavelength as a function of the size d. The dashed lines in (d) and (e) indicate the plasmon resonance in the electrostatic limit. The dielectric constant of the background is fixed at 6.145.

Unlike the case of nonlossy systems, in which the denominator is zero at $\epsilon = -2\epsilon_B$, in our system at the eigenvalue ϵ the denominator can be made equal to zero if we assume an effective complex dielectric constant of the background given by $\epsilon_B^{\text{eff}}(= \epsilon_{B,r}^{\text{eff}} + i\epsilon_{B,i}^{\text{eff}})$. Additionally, since $\text{Im}(\epsilon)$ is less than 0 in this particular system, $\epsilon_{B,i}^{\text{eff}}$ has to be positive. Therefore, at the eigenwavelength the system behaves as if the background had finite losses for larger particles. The progressive decrease in $\text{Im}(\epsilon)$ and its negative sign upon increasing the size indicates the increase of damping, both intrinsic and radiative, in the system.

B. Nanoparticle Dimer

Consider a nanoparticle dimer as shown in Fig. 2(a) in which two gold nanoparticles, each with diameter d, are separated by a gap g. Figures 2(b) and 2(c) show the computed λ_r and λ_i of this system for various particle sizes with the gap fixed at 4 nm gap. For any given particle size, four distinct modes can be identified [55,56]. As the particle size is increased, the wavelength λ_r of modes 1 and 2 shows a progressive increase. In the case of modes 3 and 4, λ_r first shows a blueshift for $d <$ 15 nm and then a redshift for larger values of d. The wider spectral separation of the eigenmodes for larger particle sizes clearly indicates the increase in the coupling between the particles due to greater field overlap. The imaginary part of the
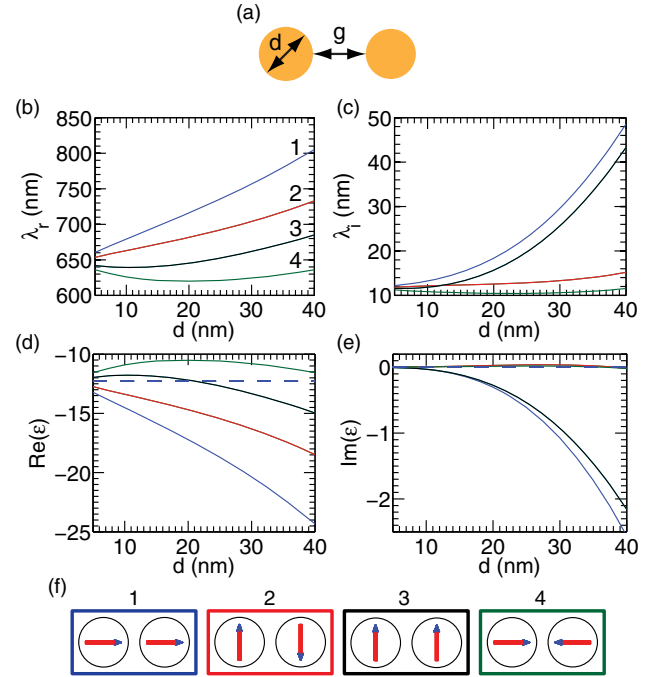

Fig. 2.   (a) Schematic of the nanoparticle dimer. (b) Real and (c) imaginary parts of the eigenwavelengths as a function of particle size d. (d) Real and (e) imaginary parts of the dielectric constant of gold at the eigenwavelength. (f) Dipole orientations in the particles for the four distinct eigenmodes depicted in (b). The direction of the arrow indicates the dipole orientation with the blue head pointing toward the negative charge. Other parameters are $g = 4$ nm and $\epsilon_B = 6.145$.

eigenwavelength, however, shows a totally different character. In the case of modes 1 and 3, a progressive increase is seen, whereas for modes 2 and 4 it does not change significantly. These differences can be understood by studying the dipole orientations for the four modes, as shown in Fig. 2(f). These dipole orientations were obtained using the eigenvector of the matrix $\mathbf{S}$ at the corresponding eigenvalues, and it must be mentioned here that the dipole orientations for the modes are independent of the nanoparticle size. In the case of modes 1 and 4, the dipole moments of the particles align along the axis joining the two dipoles, whereas for modes 2 and 3 the dipoles are oriented perpendicular to the axis [55,56]. Additionally, in modes 1 and 3 the dipoles of the two particles are parallel, whereas in modes 2 and 4 they are antiparallel. Due to the symmetry about the axis joining the two particles, modes 2 and 3 are doubly degenerate. The net zero dipole moment for modes 2 and 4 prevents them from being excited using plane wave excitation, and these modes are referred to as "dark modes" [55,56]. This is because the light scattered by the first particle will destructively interfere with the light scattered by the second particle. On the other hand, modes 1 and 3 exhibit a net dipole moment that allows them to interact with the far field and are commonly known as "bright modes." In contrast to modes 2 and 4, where destructive interference occurs, for modes 1 and 3 the particles scatter light in phase and we observe constructive interference. The imaginary part of the eigenwavelength, which corresponds to the half-width of the plasmon resonance, contains contributions from intrinsic damping (mainly caused by ohmic losses for gold) and radiative damping (due to the

radiation of light into the far field). Since modes 1 and 3 are radiative, they exhibit a much higher value of λ_i as compared to modes 2 and 4 for large particle sizes ($d > 15$ nm). This is further substantiated by the fact that as the particle size is reduced, thereby reducing the radiative damping, the values of λ_i for the modes become similar.

Figures 2(d) and 2(e) show Re(ϵ) and Im(ϵ) at the various eigenwavelengths as a function of the particle size. Re(ϵ) and Im(ϵ) show trends analogous to those of λ_r and λ_i, respectively. The Im(ϵ) for modes 1 and 3, the bright modes, progressively becomes more negative as the particle size is increased. On the other hand, for modes 2 and 4, the Im(ϵ) is positive and close to zero for all particle sizes. For modes 3 and 4 the intrinsic damping for a given particle size is similar due to the proximity of their eigenwavelengths. However, the total damping for the two modes as shown by the value of λ_i is very different. This difference is due to the presence of radiative damping in the case of mode 3, which significantly increases the value of λ_i for larger particles as compared to mode 4. As explained in the case of a single nanoparticle, the imaginary part of the dielectric constant at the eigenwavelength can be understood as the effective background possessing a finite loss if Im(ϵ) < 0. Applying a similar argument, we see that only in the case of modes 1 and 3 does the dielectric constant possess a negative value of Im(ϵ), and correspondingly the background acts as a lossy medium, which can extract light from these two modes at the eigenwavelengths. However, the positive Im(ϵ) for modes 2 and 4 shows that for these two modes, the effective background acts like a gain medium and therefore cannot act as a sink for light.

We now study the effect of varying the gap size in the case of a dimer made up of 20 nm particles. Figure 3 shows the eigenwavengths and the corresponding epsilon as a function of the inter particle gap. First, the splitting between the various modes, i.e., λ_r and Re(ϵ), decreases upon increasing the gap because of reduced coupling. For gaps close to 60 nm, λ_r and Re(ϵ) approach the values of an isolated 20 nm particle. As mentioned previously, modes 1 and 3 exhibit a negative value of Im(ϵ) for all values of the gap. However, Im(ϵ) of

modes 2 and 4 crosses zero at 30 and 48 nm gaps, respectively. This means that beyond these gap values the modes start radiating due to retardation effects. Consequently the background starts acting like a lossy medium.

C. Nanoparticle Trimer

Let us now consider a nanoparticle trimer made up of 20 nm particles as shown in Fig. 4(a). In the case of an equilateral structure ($\Delta x = 0$ nm) the gap between the particles is 4 nm. Figures 4(b)–4(d) show the variation of λ_r as a function of the displacement Δx of the top particle (P1) in the horizontal direction. As expected at most nine modes are seen for a given Δx [57]. The colored dots in Fig. 4 depict the excitation strengths of the various modes upon illumination with a polarized plane wave. For example, Fig. 4(b) shows the excitation strength of the modes due to a plane wave propagating in the z direction and polarized along the x axis. The excitation strengths are computed by the summation of the overlap of the incident field with the field of a given mode. The summation is performed over all the dipoles in the system. Similarly, Figs. 4(c) and 4(d) show the excitation strength for plane waves propagating along the z and x directions, respectively, and polarized along y and z, respectively. As Δx is increased from 0 to 12 nm, the spectral splitting between the modes (in-plane or out-of-plane modes) increases due to increased coupling. Maximum coupling is observed around $\Delta x = 12$ nm when the structure closely resembles a right-angled trimer. This is because for $\Delta x = 12$ nm the separation between particles P1 and P2 is minimized resulting in a greater field overlap. Upon further increasing Δx the splitting between the modes reduces as the separation between particles P1 and P3 becomes larger. In addition to the spectral splitting, the excitation strengths are also strongly dependent on Δx. For example, the excitation strength of the mode at the highest wavelength (mode 1) progressively increases upon increasing
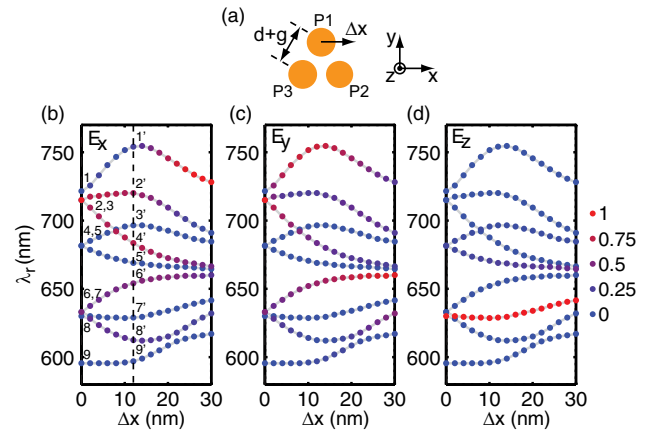
Fig. 4. (a) Schematic of the nanoparticle trimer. (b) Real part of the eigenwavelength and the corresponding excitation strengths as a function of the displacement Δx. The incident condition is a plane wave propagating in the z direction and polarized along the x axis. (c) Real part of eigenwavelength and the corresponding excitation strengths as a function of the displacement Δx. The incident condition is a plane wave propagating in the z direction and polarized along the y axis. (d) Real part of eigenwavelength and the corresponding excitation strengths as a function of displacement, Δx. The incident condition is a plane wave propagating in the x direction and polarized along the z axis. Other parameters are $d = 20$ nm, $g = 4$ nm, and $\epsilon_B = 6.145$.
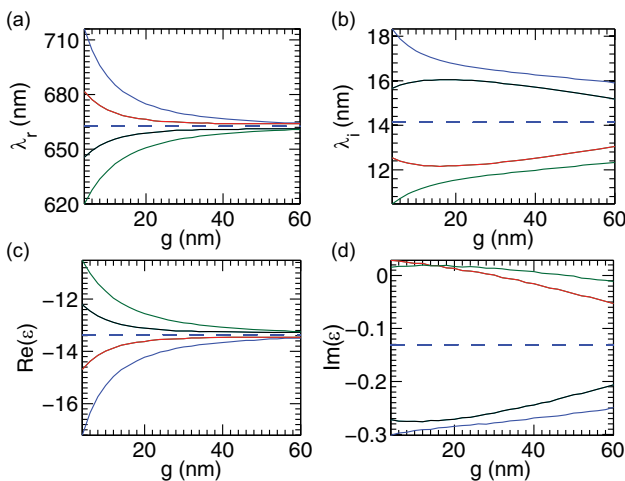
Fig. 3. (a) Real and (b) imaginary parts of the eigenwavelength for a nanoparticle dimer as a function of the gap g. (c) Real and (d) imaginary parts of the dielectric constant of gold at the corresponding eigenwavelength as a function of the gap g. Other parameters are $d = 20$ nm and $\epsilon_B = 6.145$. The dashed lines show the value of the corresponding parameter for a single 20 nm particle.
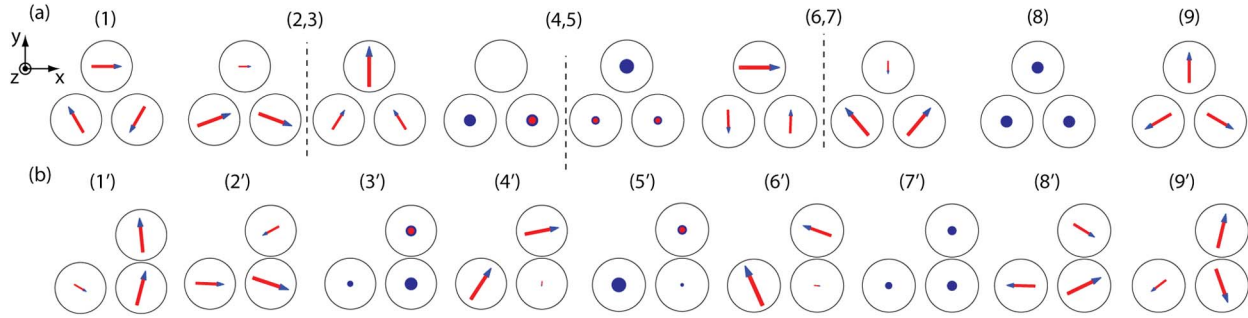
Fig. 5.   (a) Field distribution of the various eigenmodes of an equilateral trimer ($\Delta x = 0$ nm). Degenerate eigenmodes have been clubbed together for clarity. The number of the modes is also shown in Fig. 4(b) for clarity. (b) Field distribution of the various eigenmodes of a trimer ($\Delta x = 12$ nm). The numbers of the modes are also shown in Fig. 4(b) for clarity. The direction of the arrow indicates the electric field orientation with the blue head pointing toward the negative charge. A solid blue circle indicates the electric field pointing in the $+z$ direction, and a hollow blue circle with a red dot indicates the electric field pointing in the $-z$ direction.

Δx in the case of an x polarized plane wave. In contrast, for y polarized plane wave excitation, this mode is best excited at $\Delta x = 12$ nm.

To better understand the behavior of this system we correlate the excitation strengths of the various modes with their dipole distributions. The field distributions of the modes of an equilateral trimer, $\Delta x = 0$ nm, are shown in Fig. 5(a). This system has six modes with the dipoles oriented in the plane of the structure (modes 1, 2, 3, 6, 7, and 9), whereas for three modes the dipoles are oriented perpendicular to the plane of the structure (modes 4, 5, and 8). Furthermore, due to the symmetry of the structure it has three pairs of doubly degenerate modes [modes (2,3), (4,5), and (6,7)]. Clearly, modes 1, 4, 5, and 9 have a zero net dipole moment and cannot be excited using plane wave excitation. This is also evident from Figs. 4(b)–4(d) whereby the excitation strength of these modes is zero regardless of the light polarization. On the other hand, modes 2, 3, 6, and 7 possess a net dipole moment in the xy plane and can be excited using an x or y polarized plane wave. Mode 8, however, exhibits a net dipole moment along the z direction and can only be excited using a plane wave polarized along the z direction. Note that modes 2, 3, 6, and 7 cannot be excited with a z polarized plane wave and are thus "dark modes" for this given polarization. This is also depicted in Fig. 4(d), where these modes exhibit a zero excitation strength. Analogously, since mode 8 cannot be excited using an x or y polarized plane wave, it acts like a "dark mode" for these polarizations and shows a zero excitation strength [Figs. 4(b) and 4(c)].

As the particle P1 is displaced in the x direction, the symmetry of the structure breaks and consequently we observe that the degeneracy of the modes, present in case of the equilateral structure, is lifted. As mentioned previously the spectral separation between the in-plane modes (1, 2, 3, 6, 7, and 9) and out-of-plane modes (4, 5 and 8) increases for $\Delta x < 12$ nm and then decreases. For example, the mode 2 and 3 (for $\Delta x = 0$ nm) splits into two modes (leading to modes 2′ and 4′ for a structure with $\Delta x = 12$ nm). Each of these split modes shows different excitation strengths for different values of Δx. For an x polarized plane wave, both the split modes show comparable excitation strengths for $\Delta x < 12$ nm, but for larger values of Δx mode 4′ is excited more efficiently [Figs. 4(b) and 5(b)]. This is because in the case of mode 2′ as the particle P1 is displaced, its dipole moment along the x axis progressively increases. In addition, the dipole of

particle P1 is aligned opposite to the dipoles of particles P2 and P3, which reduces the net dipole moment and lowers the excitation strength of the mode. In the case of mode 4′ the dipoles of particles P1 and P3 are predominantly excited and they are always in phase considering the x axis; therefore this mode exhibits larger excitation strengths even for larger values of Δx [Figs. 4(b) and 5(b)]. In contrast for y polarized light mode 4′ demonstrates a higher excitation strength as compared to mode 2′ for $\Delta x < 12$ nm [Fig. 4(c)]. Larger values of Δx lead to comparable excitation strengths of modes 2′ and 4′. This behavior can again be traced back to the field distributions. Mode 2′ shows a near-zero dipole moment along the y direction and consequently a near-zero excitation strength [Fig. 5(b)]. Similar mode splittings are also observed in the case of modes (4,5) and modes (6,7) of the equilateral structure upon displacement of particle P1. Figure 5(b) shows the field distributions for a particular symmetry broken nanoparticle trimer with $\Delta x = 12$ nm, which manifests maximal coupling in the system. In this case, none of the modes are degenerate and the system has nine distinct modes. In this case, all the in-plane modes, 1′, 2′, 4′, 6′, 8′, and 9′, show a nonzero dipole moment along both the x and y axes and a nonzero excitation strength [Figs. 4(b) and 4(c)]. These modes can thus be excited using a plane wave with polarization in the plane of the structure. On the other hand, the out-of-plane modes, modes 3′, 5′, and 7′, show a net nonzero dipole moment along the z axis and thus can be excited using a z polarized plane wave. However, even in this case, the in-plane
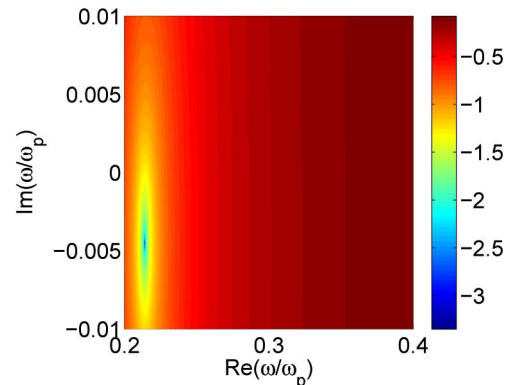

Fig. 6. $\log_{10}|\xi - 1|$ plotted as a function of the real and imaginary parts of the normalized frequency ω/ω_p.

modes are "dark modes" for a z polarized plane wave, and the out-of-plane modes are "dark modes" for x or y polarized plane waves.

4. CONCLUSION

A method based on the Green's tensor technique for computing the eigenmodes of a plasmonic system composed of nanoparticles has been developed. Using examples of monomers, dimers, and trimers, we have shown that the modes exhibit complex eigenwavelengths. The effect of various geometrical parameters on the complex eigenwavelengths has been studied in detail. In the case of a dimer, it was shown that the imaginary part of the dielectric constant of the plasmonic metal at the eigenwavelengths indicates the contributions of radiative and intrinsic damping in that mode. Finally, the effect of symmetry breaking was studied for the case of a nanoparticle trimer by monitoring both the eigenwavelengths and the excitation strengths of the modes by various incident conditions. The different resulting modes were classified in terms of their net dipole moment, thereby providing indications on which modes can be excited under specific illumination conditions.

APPENDIX A

In this appendix we briefly show that the same results are obtained when performing the eigenmode analysis using the frequency as the eigenvalue, instead of the wavelength, as done in the main text. Figure 6 shows the variation of $\log_{10}|\xi - 1|$ as a function of $\text{Re}(\omega/\omega_p)$ and $\text{Im}(\omega/\omega_p)$ for a 20 nm gold nanoparticle suspended in a medium with $\epsilon_B = 6.145$. As explained previously, the equation $\xi(\omega) = 1$ is satisfied for $\omega = (0.2091 - 0.0045i)\omega_p$, which is the eigenfrequency of the single particle. Correspondingly, $\lambda = 662 + 14i$, which is exactly the same eigenwavelength as computed earlier. Thus, eigenmode analysis with frequency as the eigenvalue is identical to the analysis performed using wavelength as the eigenvalue.

ACKNOWLEDGMENTS

REFERENCES

1. D. Graham and R. Goodacre, "Chemical and bioanalytical applications of surface enhanced Raman scattering spectroscopy," Chem. Soc. Rev. **37**, 883–884 (2008).
2. J. Kneipp, H. Kneipp, and K. Kneipp, "SERS a single-molecule and nanoscale tool for bioanalytics," Chem. Soc. Rev. **37**, 1052–1060 (2008).
3. X.-M. Qian and S. M. Nie, "Single-molecule and single-nanoparticle SERS: from fundamental mechanisms to biomedical applications," Chem. Soc. Rev. **37**, 912–920 (2008).
4. W. Zhang, H. Fischer, T. Schmid, R. Zenobi, and O. J. F. Martin, "Mode-selective surface-enhanced Raman spectroscopy using nanofabricated plasmonic dipole antennas," J. Phys. Chem. C **113**, 14672–14675 (2009).
5. A. M. Kern, A. J. Meixner, and O. J. F. Martin, "Molecule-dependent plasmonic enhancement of fluorescence and Raman scattering near realistic nanostructures," ACS Nano **6**, 9828–9836 (2012).
6. J. N. Anker, W. P. Hall, O. Lyandres, N. C. Shah, J. Zhao, and R. P. Van Duyne, "Biosensing with plasmonic nanosensors," Nat. Mater. **7**, 442–453 (2008).
7. K. M. Mayer and J. H. Hafner, "Localized surface plasmon resonance sensors," Chem. Rev. **111**, 3828–3857 (2011).
8. B. Gallinet and O. J. F. Martin, "Refractive index sensing with subradiant modes: a framework to reduce losses in plasmonic nanostructures," ACS Nano **7**, 6978–6987 (2013).
9. B. Abasahl, S. Dutta-Gupta, C. Santschi, and O. J. F. Martin, "Coupling strength can control the polarization twist of a plasmonic antenna," Nano Lett. **13**, 4575–4579 (2013).
10. L. Huang, S. J. Maerkl, and O. J. Martin, "Integration of plasmonic trapping in a microfluidic environment," Opt. Express **17**, 6018–6024 (2009).
11. A. Lovera and O. J. F. Martin, "Plasmonic trapping with realistic dipole nanoantennas: analysis of the detection limit," Appl. Phys. Lett. **99**, 151104 (2011).
12. W. Zhang, L. Huang, C. Santschi, and O. J. F. Martin, "Trapping and sensing 10 nm metal nanoparticles using plasmonic dipole antennas," Nano Lett. **10**, 1006–1011 (2010).
13. O. L. Muskens, V. Giannini, J. A. Sanchez-Gil, and J. Gomez Rivas, "Strong enhancement of the radiative decay rate of emitters by single plasmonic nanoantennas," Nano Lett. **7**, 2871–2875 (2007).
14. G. Colas des Francs, A. Bouhelier, E. Finot, J. C. Weeber, A. Dereux, C. Girard, and E. Dujardin, "Fluorescence relaxation in the near–field of a mesoscopic metallic particle: distance dependence and role of plasmon modes," Opt. Express **16**, 17654–17666 (2008).
15. M. Ringler, A. Schwemer, M. Wunderlich, A. Nichtl, K. Kurzinger, T. A. Klar, and J. Feldmann, "Shaping emission spectra of fluorescent molecules with single plasmonic nanoresonators," Phys. Rev. Lett. **100**, 203002 (2008).
16. G. Baffou, C. Girard, E. Dujardin, G. Colas des Francs, and O. J. F. Martin, "Molecular quenching and relaxation in a plasmonic tunable system," Phys. Rev. B **77**, 121101 (2008).
17. J. Lakowicz and Y. Fu, "Modification of single molecule fluorescence near metallic nanostructures," Laser Photonics Rev. **3**, 221–232 (2009).
18. P. Mandal, A. Singh, S. Kasture, A. V. Gopal, and A. Vengurlekar, "Plasmon assisted intense blue-green emission from ZnO/ZnS nanocrystallites," Opt. Mater. **33**, 1786–1791 (2011).
19. Y. Tsuji, "Finite element method using port truncation by perfectly matching layer boundary conditions for optical waveguide discontinuity problems," J. Lightwave Technol. **20**, 463–468 (2002).
20. A. Downes, D. Salter, and A. Elfick, "Finite element simulations of tip-enhanced Raman and fluorescence spectroscopy," J. Phys. Chem. B **110**, 6692–6698 (2006).
21. J. M. McMahon, A. I. Henry, K. L. Wustholz, M. J. Natan, R. G. Freeman, R. P. Van Duyne, and G. C. Schatz, "Gold nanoparticle dimer plasmonics: finite element method calculations of the electromagnetic enhancement to surface-enhanced Raman spectroscopy," Anal. Bioanal. Chem. **394**, 1819–1825 (2009).
22. O. J. F. Martin and N. B. Piller, "Electromagnetic scattering in polarizable backgrounds," Phys. Rev. E **58**, 3909–3915 (1998).
23. P. Gay-Balmaz and O. J. Martin, "Validity domain and limitation of non-retarded Green's tensor for electromagnetic scattering at surfaces," Opt. Commun. **184**, 37–47 (2000).
24. M. Paulus and O. J. Martin, "Green's tensor technique for scattering in two-dimensional stratified media," Phys. Rev. E **63**, 066615 (2001).
25. B. T. Draine and P. J. Flatau, "Discrete-dipole approximation for scattering calculations," J. Opt. Soc. Am. A **11**, 1491–1499 (1994).
26. B. T. Draine and P. J. Flatau, "Discrete-dipole approximation for periodic targets: theory and tests," J. Opt. Soc. Am. A **25**, 2693–2703 (2008).
27. F. J. Garcia de Abajo, "Optical excitations in electron microscopy," Rev. Mod. Phys. **82**, 209–275 (2010).
28. F. J. Garcia de Abajo and A. Howie, "Retarded field calculation of electron energy loss in inhomogeneous dielectrics," Phys. Rev. B **65**, 115418 (2002).
29. U. Hohenester and A. Trugler, "MNPBEM—a Matlab toolbox for the simulation of plasmonic nanoparticles," Comput. Phys. Commun. **183**, 370–381 (2012).
30. J. Makitalo, S. Suuriniemi, and M. Kauranen, "Boundary element method for surface nonlinear optics of nanoparticles," Opt. Express **19**, 23386–23399 (2011).

31. A. M. Kern and O. J. F. Martin, "Surface integral formulation for 3D simulations of plasmonic and high permittivity nanostructures," J. Opt. Soc. Am. A **26**, 732–740 (2009).

32. A. M. Kern and O. J. F. Martin, "Pitfalls in the determination of optical cross sections from surface integral equation simulations," IEEE Trans. Antennas Propag. **58**, 2158–2161 (2010).

33. B. Gallinet, A. M. Kern, and O. J. F. Martin, "Accurate and versatile modeling of electromagnetic scattering on periodic nanostructures with a surface integral approach," J. Opt. Soc. Am. A **27**, 2261–2271 (2010).

34. O. J. F. Martin, A. Dereux, and C. Girard, "Iterative scheme for computing exactly the total field propagating in dielectric structures of arbitrary shape," J. Opt. Soc. Am. A **11**, 1073–1080 (1994).

35. J. Grandidier, S. Massenot, G. C. des Francs, A. Bouhelier, J.-C. Weeber, L. Markey, A. Dereux, J. Renger, M. U. González, and R. Quidant, "Dielectric-loaded surface plasmon polariton waveguides: figures of merit and mode characterization by image and Fourier plane leakage microscopy," Phys. Rev. B **78**, 245419 (2008).

36. G. Colas des Francs, J. Grandidier, S. Massenot, A. Bouhelier, J.-C. Weeber, and A. Dereux, "Integrated plasmonic waveguides: a mode solver based on density of states formulation," Phys. Rev. B **80**, 115419 (2009).

37. M. Iwanaga, "Electromagnetic eigenmodes in a stacked complementary plasmonic crystal slab," Phys. Rev. B **82**, 155402 (2010).

38. I. A. Ibrahim, M. Mivelle, T. Grosjean, J. T. Allegre, G. W. Burr, and F. I. Baida, "Bowtie-shaped nanoaperture: a modal study," Opt. Lett. **35**, 2448–2450 (2010).

39. C.-Y. Tai, W.-H. Yu, and S. H. Chang, "Giant angular dispersion mediated by plasmonic modal competition," Opt. Express **18**, 24510–24515 (2010).

40. W. Zhang, B. Gallinet, and O. J. F. Martin, "Symmetry and selection rules for localized surface plasmon resonances in nanostructures," Phys. Rev. B **81**, 233407 (2010).

41. H. Guo, B. Oswald, and P. Arbenz, "3-dimensional eigenmodal analysis of plasmonic nanostructures," Opt. Express **20**, 5481–5500 (2012).

42. T. Sandu, "Eigenmode decomposition of the near-field enhancement in localized surface plasmon resonances of metallic nanoparticles," Plasmonics **8**, 391–402 (2013).

43. G. Volpe, G. Molina-Terriza, and R. Quidant, "Deterministic subwavelength control of light confinement in nanostructures," Phys. Rev. Lett. **105**, 216802 (2010).

44. S.-O. Guillaume, F. J. G.-a. de Abajo, and L. Henrard, "Efficient modal-expansion discrete-dipole approximation: application to the simulation of optical extinction and electron energy-loss spectroscopies," Phys. Rev. B **88**, 245439 (2013).

45. T. J. Davis, D. E. Gomez, and K. C. Vernon, "Simple model for the hybridization of surface plasmon resonances in metallic nanoparticles," Nano Lett. **10**, 2618–2625 (2010).

46. E. Prodan, C. Radloff, N. J. Halas, and P. Nordlander, "A hybridization model for the plasmon response of complex nanostructures," Science **302**, 419–422 (2003).

47. R. Fuchs, "Theory of the optical properties of small cubes," Phys. Lett. A **48**, 353–354 (1974).

48. R. Fuchs, "Theory of the optical properties of ionic crystal cubes," Phys. Rev. B **11**, 1732–1740 (1975).

49. N. Grady, N. Halas, and P. Nordlander, "Influence of dielectric function properties on the optical response of plasmon resonant metallic nanoparticles," Chem. Phys. Lett. **399**, 167–171 (2004).

50. A. D. Rakic, A. B. Djurisic, J. M. Elazar, and M. L. Majewski, "Optical properties of metallic films for vertical-cavity optoelectronic devices," Appl. Opt. **37**, 5271–5283 (1998).

51. J. A. Dionne, L. A. Sweatlock, H. A. Atwater, and A. Polman, "Planar metal plasmon waveguides: frequency-dependent dispersion, propagation, localization, and loss beyond the free electron model," Phys. Rev. B **72**, 075405 (2005).

52. H. Goldstein, C. H. J. Poole, and J. L. Safko, *Classical Mechanics*, 3rd ed. (Addison Wesley, 2000).

53. M. Tooley and M. Tooley, *Electronic Circuits: Fundamentals and Applications*, 3rd ed. (Elsevier, 2006).

54. M. Zhang, G. Lin, C. Dong, and L. Wen, "Amorphous TiO_2 films with high refractive index deposited by pulsed bias arc ion plating," Surf. Coat. Technol. **201**, 7252–7258 (2007).

55. P. Nordlander, C. Oubre, E. Prodan, K. Li, and M. I. Stockman, "Plasmon hybridization in nanoparticle dimers," Nano Lett. **4**, 899–903 (2004).

56. I. Romero, J. Aizpurua, G. W. Bryant, and F. J. G. D. Abajo, "Plasmons in nearly touching metallic nanoparticles: singular response in the limit of touching dimers," Opt. Express **14**, 9988–9999 (2006).

57. D. W. Brandl, N. A. Mirin, and P. Nordlander, "Plasmon modes of nanosphere trimers and quadrumers," J. Phys. Chem. B **110**, 12302–12310 (2006).